Available online at www.sciencedirect.com

ScienceDirect

journal homepage: www.elsevier.com/locate/he

SEM and XAS characterization at beginning of life of Pd-based cathode electrocatalysts in PEM fuel cells

K. Suarez-Alcantara [a,b,*], D.C. Martínez-Casillas [c], K.B. Zheng [d], Q. Zhu [a], M. Abdellah [d,e], D. Haase [f], T. Pullerits [d], O. Solorza-Feria [c], S.E. Canton [a]

[a] Department of Synchrotron Radiation Instrumentation, Lund University, Ole Römers väg 1, SE-22363 Lund, Sweden
[b] UNAM IIM-Morelia, Antigua Carretera a Pátzcuaro No. 8701, Col. Ex Hacienda de San José de la Huerta, C.P. 58190, Morelia, Michoacán, México
[c] Center of Research and Advanced Studies (CINVESTAV), A. Postal 14-740, 07360 México DF, Mexico
[d] Department of Chemical Physics, Lund University, Box 124, 22100 Lund, Sweden
[e] Department of Chemistry, Qena Faculty of Science, South Valley University, Qena 83523, Egypt
[f] MAX IV Laboratory, Lund University, Ole Römers väg 1, SE-22363 Lund, Sweden

ARTICLE INFO

Article history:
Received 1 October 2013
Received in revised form
6 January 2014
Accepted 9 January 2014
Available online 15 February 2014

Keywords:
Synchrotron radiation
Electrocatalyst
Fuel cell
Pd nanoparticles

ABSTRACT

The fuel cell performance of membrane electrode assemblies with a Pt anode and Pd, PdCu or Pd_5Cu_4Pt cathodes has been tested during 116 h (beginning of life). The incorporation of Cu to Pd increases the fuel cell performance. Incorporation of Pt leads to further improvement. SEM micrographs of the as-prepared and the fuel cell-tested assemblies show the effects of the 116 h of continuous operation. Nafion membranes were characterized by small angle X-ray scattering. The results show a reduction of the size of the lamellar domains in the perfluorinated matrix after fuel cell testing, but no correlation with the cathode electrocatalyst material. The cathode electrocatalysts were characterized by ex-situ synchrotron radiation X-ray diffraction and X-ray absorption spectroscopy at the Pd L_3, Cu K and Pt L_3 edges. Re-organization of Pd_5Cu_4Pt electrocatalyst after fuel cell testing was observed. The Cu in the electrocatalyst can be described as a nano-mixture of metallic Cu, alloyed Cu and CuO. The CuO acts as a promoter of the ORR.

1. Introduction

Polymer electrolyte membrane fuel cells (PEMFCs) are efficient electrical power sources for vehicles and stationary applications. The electrochemical reactions that govern their performance take place within the membrane electrode assembly (MEA), which consists of three layers. The central one is a proton-conductive membrane. The two outer ones, i.e. the electrode layers anode and cathode, are composed of a mixture of electrocatalyst (nanoparticles) supported by high surface area carbon embedded in a proton-conductive polymer [1]. At the cathode side, the oxygen reduction reaction (ORR) happens, $O_2 + 4H^+ + 4e^- \rightarrow 2H_2O$. At the anode side, the hydrogen oxidation reaction (HOR) takes place, $2H_2 \rightarrow 4H^+ + 4e^-$. Layer by layer, the main MEA components are studied in the present work. The aim was to investigate

* *Corresponding author*. UNAM-IIM Morelia, Antigua carretera a Pátzcuaro 8710, Col. Ex-hacienda de San José de la Huerta, Morelia, Michoacán 58190, Mexico. Tel.: +52 4433222777.
E-mail address: karina_suarez@iim.unam.mx (K. Suarez-Alcantara).
0360-3199/$ – see front matter
http://dx.doi.org/10.1016/j.ijhydene.2014.01.056

the stability of the MEA components after 116 h of continuous fuel cell operation; i.e. beginning of life (BOL). Measurements were done on as-prepared MEAs and after 116 h of fuel cell operation.

The central layer: The proton exchange membrane (PEM) can have an important effect on the fuel cell performance. The PEM stability is directly linked to the formation of HO• and HOO• radicals [2] and the contamination of metal cations from the dissolution of the electrocatalysts. The production of radicals is ruled by the cathode electrocatalyst; the radicals are recognized as being side products of the ORR. Description of the changes of the MEA after fuel cell operation is only completed by the proper morphological characterization of the PEM. Small angle X-ray scattering (SAXS) and scanning electron microscopy (SEM) are particularly useful to determine the structural features of the PEM [3].

The electrocatalysts layers: Pt and its alloys are the most common electrocatalysts for PEMFCs, both for the anode and cathode. Studies have been focused on minimizing the amount of Pt used (especially for cathodes that use high loading) or to replace it totally with less expensive materials. Recently Pd and Pd-alloys have been attracting attention as cathode electrocatalysts since they are less expensive than Pt. Pd and Pd-alloys have appreciable activity towards the ORR [4]. Pd, PdCu and Pd_5Cu_4Pt nanoparticles synthesized by a chemical reduction method with $NaBH_4$ in a tetrahydrofuran (THF) solution have demonstrated high activity towards the ORR in acid media [5,6]. Fuel cell testing of Pd_5Cu_4Pt nanoparticles as cathode electrocatalyst has shown performances comparable with commercial Pt nanoparticles [7]. The origin of the activity, albeit already proposed to be strongly connected to Pd and Pt *d*-orbitals, remains to be explained. Particularly the role of Cu is to be revealed. It may play a role as an active phase, an inert diluent, or stabilizing Pd or Pd–Pt against sintering processes during the fuel cell operation. In the present work X-ray absorption at Pd L_3-edge, Cu K-edge and Pt L_3-edge has been performed directly on the MEAs. The complementary nature of multi-edge analysis is helpful in the characterization of such complex systems. These ex-situ experiments reveal the changes in the Pd and Pt *d*-orbital occupancy upon catalyst formation.

2. Experimental details

2.1. Electrocatalysts synthesis

Nanosized crystalline Pd, PdCu and Pd_5Cu_4Pt were produced by reduction of the corresponding salts with $NaBH_4$ in 100 mL THF, as reported elsewhere [5–7]. All salts were purchased from Aldrich and used without purification. Briefly, the reaction system was charged with $PdCl_2$ (0.86 mM); $PdCl_2$ (11.76 mM) and CuCl (12.0 mM) or $PdCl_2$ (6.9 mM), CuCl (5.5 mM) and H_2PtCl_6 (1.3 mM) in dry THF. The reducing agent, $NaBH_4$ (0.03 mM, 42.6 mM and 33 mM respectively) in dry THF, was then slowly added drop by drop. After reduction, the nanoparticles were washed, filtered, and dried. Then, the Pd, PdCu and Pd_5Cu_4Pt nanoparticles were supported on carbon Vulcan: the Pd, PdCu or Pd_5Cu_4Pt nanoparticles plus the appropriate amount of carbon Vulcan to give a load of 40 wt% were mixed with ethanol in an ultrasonic bath, then the mixture was dried and stored.

2.2. MEA preparation and performance characterization

In short, the electrocatalyst/carbon Vulcan/ethanol/Nafion suspension or "catalytic ink" was sprayed and hot-pressed over an activated Nafion 117 membrane. The activation process of Nafion membranes includes the successive hot-soaking in H_2SO_4 2 M, distillated water, H_2O_2 3%vol. and distillated water at 80 °C (1 h each soaking) [8]. The membranes were stored in distillated water at room temperature until MEA preparation. 10 mg of the carbon-supported Pd, PdCu or Pd_5Cu_4Pt were mixed with 83 μL of Nafion ionomer and 1.5 mL of ethanol to form the cathode-catalytic ink. The catalytic-inks were sprayed over a membrane area of 5 cm^2 by means of a home-developed automatized catalytic printer. In this way the homogeneity and reproducibility of the MEAs were guaranteed. For the anode side, commercial Pt nanoparticles dispersed in carbon cloth were used (Pt/C, ETEK, 20 wt% with loading of 0.5 mg cm^{-2}). A porous carbon cloth was attached to the cathode side as diffusion layer, then the MEAs were hot-pressed at 120 °C and 11 kg cm^{-2} for 2 min. In total six MEAs were produced as three twin pairs for each type of nanoparticles.

The continuous fuel cell performance of three MEAs was determined in a commercial system Compucell GT, Electrochem 890B as described elsewhere [9]. Briefly, the fuel cell test station was operated at 100 cm^3 min^{-1} flow of high purity H_2 and O_2. The gas pressures at the anode and cathode sides were set at 2 bar. Humidification of the reactant gases was ensured by bubbling them in distillated water at 85 °C. The fuel cell performance, i.e. cell voltage current density curves were recorded at 80 °C. The complete fuel cell testing time was 116 h. This duration includes the interval for heating-up, pressure setting, electrochemical activation to steady state of electrocatalysts, and a stability test of 100 h. The stability test was accomplished by fixing the cell potential and recording the current density. The fixed cell potential corresponded approximately to the maximum power density achieved with each cathode material in the polarization curves. These were 0.3 V for MEA2 Pd-cathode, 0.4 V for MEA4 PdCu-cathode and 0.5 V for MEA6 Pd_5Cu_4Pt-cathode. Hereafter the MEAs are numbered from 1 to 6 and labeled as "new" to designate the as-prepared MEAs. Those for which the fuel cell performance was determined at the beginning of life were labeled as "BOL" MEAs. Table 1 summarizes the MEA composition and labeling. After MEA preparation (new-MEAs) or fuel cell testing (BOL-MEAs), all MEAs were dry-stored before the various characterization experiments described in the next sections.

2.3. Scanning electron microscopy (SEM) imaging

The MEAs for SEM imaging were cut as thin strips with a sharp knife. Chronologically, it was the last characterization performed on the MEAs. SEM micrographs (Gemini T607 SEM-LEO 1560) were taken at the transversal section of MEAs and at the top of cathode. Low magnification, electron accelerating

Table 1 – MEA description and continuous fuel cell performance, structural parameters, SAXS, SR-XRD and XAS.

MEA and status	Cathode electrocatalyst and load [mg electrocatalyst cm^{-2}]	Anode electrocatalyst and load [mg electrocatalyst cm^{-2}]	Fuel cell continuous performance [mW $mg^{-1}_{electrocatal}$][a]	Resistance [Ω cm^2]	SAXS fit- dry membranes		SR-XRD Unit cell size ($a = b = c$) [Å] Bond distance [Å] Nanocrystal domains size [Å]	FT-XAS FT peak position – distance to first coordination shell [Å]
					Long period lamellar Low q range (0.1–0.6 nm^{-1}) Ellipsoid particles R_a [nm] R_b [nm]	Ionic cluster domain High q range (0.6–2.99 nm^{-1}) Core-shell cylinder particles Shell thickness [nm] Core radius [nm] Core length [nm]		
MEA-1 (new)	Pd, 0.8	Pt, 0.5	–	–	12.7 ± 0.1 29.7 ± 0.3	0.3 ± 0.1 1.7 ± 0.1 5.2 ± 0.2	3.89 ± 0.01 2.75 ± 0.07 40.5 ± 3.3	
MEA-2 (BOL)	Pd, 0.8	Pt, 0.5	13.1 at 0.3 V	9.4	7.7 ± 0.1 21.7 ± 0.1	0.7 ± 0.1 1.5 ± 0.1 5.8 ± 0.1	3.89 ± 0.04 2.75 ± 0.07 23.8 ± 1.4	
MEA-3 (new)	PdCu, 0.8	Pt, 0.5	–	–	11.3 ± 0.1 30.1 ± 0.3	0.6 ± 0.1 1.6 ± 0.1 4.8 ± 0.2	3.86 ± 0.05 2.73 ± 0.07 34.8 ± 3.0	Cu K-edge: Cu–O: 1.8 Cu–Cu: 2.5
MEA-4 (BOL)	PdCu, 0.8	Pt, 0.5	21.5 at 0.4 V	8.8	11.2 ± 0.1 32.1 ± 0.1	0.5 ± 0.1 1.7 ± 0.1 4.9 ± 0.1	3.86 ± 0.02 2.73 ± 0.07 30.4 ± 3.0	Cu-M: 2.4 and 2.9
MEA-5 (new)	Pd_5Cu_4Pt, 0.8	Pt, 0.5	–	–	13.0 ± 0.1 30.2 ± 0.3	0.5 ± 0.1 1.5 ± 0.1 5.2 ± 0.1	3.83 ± 0.07 2.71 ± 0.07 30. 4 ± 3.0	Pt L_3-edge: Pt–Pt: 2.8 Pt-M: 2.5
MEA-6 (BOL)	Pd_5Cu_4Pt, 0.8	Pt, 0.5	62.5 at 0.5 V	5.1	8.9 ± 0.1 27.5 ± 0.1	0.3 ± 0.1 1.8 ± 0.1 5.1 ± 0.1	3.90 ± 0.01 2.76 ± 0.07 30.3 ± 3.0	

[a] At the cell potential of maximum of power density; all data at 80 °C and 2 bar H_2 and O_2 pressure.

voltage of 4 kV and secondary electron detector enable the imaging of the three layers of MEAs.

2.4. Small angle X-ray scattering collection

Small angle X-ray scattering (SAXS) data were collected at I911-4 beamline of MAX-Lab synchrotron facility, Sweden [10,11]. The wavelength was fixed at 0.91 Å. A bi-dimensional detector CCD (165 mar CCD) was used in the q-range of 0.1–2.99 nm^{-1}. The sample to detector distance was fixed, and the value was refined with silver behenate as reference. The X-ray beam was focused in the Nafion 117 membrane close to the electrocatalyst area. The exposure time was 360 s. Image integration, i.e. data reduction, was performed at I911-4 beamline; proper correction for air scattering and background were made. Data fitting to suitable models was performed with SansView 2.0.1.

2.5. Synchrotron radiation X-ray diffraction

The crystal features of the electrocatalysts were investigated by synchrotron radiation X-ray diffraction (SR-XRD) taken at the I711 beamline of MAX-lab synchrotron facility, Sweden [12]. The wavelength was 1.008 ± 0.03 Å. A CCD detector (Titan CCD camera) was used. An exposure time of 240 s and an appropriate rotation of the sample were set. In order to have only the contribution of the anode or cathode electrocatalyst, approximately 1 cm^2 of the electrode surface was carefully removed by scraping. The samples were packed and sealed in glass capillaries (0.3 mm diameter). Radial integration was performed with the fit2d software [13]. Data analysis was performed with the MAUD software.

2.6. X-ray absorption data collection

X-ray absorption spectroscopy (XAS) spectra were taken at the I811 beamline of MAX-Lab synchrotron facility, Sweden [14,15], over three different runs according to the edge energy. XAS spectra were recorded at the Pd L_3-edge, Cu K-edge and Pt L_3-edge in fluorescence mode. The MEAs were placed inside a He-filled chamber. The studied side of the MEA (anode or cathode) was oriented at 45° with respect to the incident beam.

Pd L_3-edge spectra were taken between −20 eV and 250 eV respective to $E_0 = 3173$ eV; with a step of 0.12 eV. 5 scans were averaged. Cu K-edge XAS spectra were taken between −50 eV and 500 eV respective to $E_0 = 8979$ eV; with a step = 0.12 eV, 2 scans were averaged. Pt L_3-edge XAS spectra were collected between −100 eV and 800 eV respective to $E_0 = 11{,}564$ eV; with a step = 0.19 eV, 10 scans were averaged. Pt L_3-edge spectra of the anodes of MEA1-new and MEA2-BOL, i.e. commercial Pt nanoparticles, were collected as reference for alloy formation and changes after fuel cell testing. Pt L_3-edge spectra of Pd_5Cu_4Pt in MEA5-new and MEA6-BOL were taken at the cathode side of the MEAs in fluorescence mode. However due to the slimness of the MEAs these spectra are the result of the additive contributions from the Pd_5Cu_4Pt at the cathode and the Pt at the anode, the latter giving the primary contribution to the signal. Complementary, Pt L_3-edge spectra of as-synthesized Pd_5Cu_4Pt powder were also collected. Approximately 1 mg of the sample was grinded in a mortar and distributed over a 1.5 cm^2 area of the glue-side of Kapton tape. Pt L_3-spectra of Pd_5Cu_4Pt powder were collected under the same conditions as for the MEAs. The data were processed with the Athena program [16].

3. Results and discussion

3.1. Fuel cell 100 h performance

The fuel cell continuous performance at the BOL is plotted in Fig. 1. Table 1 summarizes the performance as a function of electrocatalyst load and cell potential. The incorporation of Cu into the Pd matrix clearly leads to an increase in performance. The presence of Pt in the Pd_5Cu_4Pt electrocatalyst results into a two-fold improvement of the fuel cell performance. When compared to pure Pt, this material presents a reduction of Pt load by substituting 90% of the Pt atoms by Pd and Cu. In this regard, the materials fulfill the intended objective of reducing Pt load, while keeping adequate fuel cell performance. Minor changes in the observed current density during the 100 h testing can be ascribed to small variations in the flow-in of gases and flow-out of water. However, there is a clear tendency towards the stabilization of the observed current density. The 100 h continuous fuel cell electrochemical activity confirms the reported findings from ORR electro-kinetics taken by means of rotating disk electrode [5,6,17]. There, a clear increase in the open circuit potential E_{ocp} (that in turn affects the operating cell potential) and exchange current density j_0 were observed with the addition of Cu and Cu–Pt to the Pd nanoparticles (Table 2).

In addition to electrocatalyst activity, the fuel cell performance also depends upon the resistance losses: activation, ohmic and concentration. The activation losses at low current densities are due to the sluggish kinetics of the ORR. The ohmic losses are typically attributed to the resistance of the

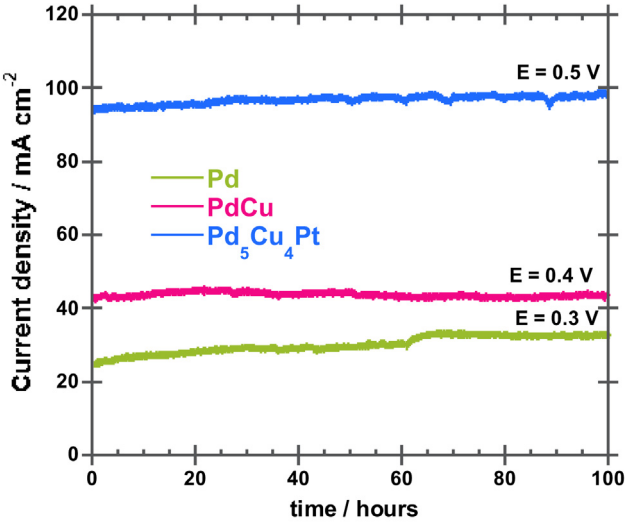

Fig. 1 – PEM fuel cell performance continuous testing at 80 °C. Beginning of life (BOL). Gas pressures at the anode and cathode sides set at 2 bar, 100 cm^3 min^{-1} flowing.

Table 2 – Kinetic Parameter E_{ocp} and j_0 from ORR at 25 °C and H_2SO_4 0.5 M; Fuel cell performance, same cathode and anode load as in Table 1, all data at 80 °C and 2 bar H_2 and O_2 pressure.

Electrocatalyst	E_{ocp} [V]	j_0 [mA cm^{-2}]	Maximum fuel cell power density [mW cm^{-2}] [mW mg$^{-1}_{electrocatal}$]	E_{ocp} at fuel cell [V][a]	Ohmic resistance [Ω cm^2][a]
Pt	0.95 [6]	5.05×10^{-4} [6]	350 at 0.45 V [17] 437.5	0.99	0.53
Pd	0.80 [5,6]	3.00×10^{-6} [6] 6.60×10^{-6} (at 30 °C) [5]	40 at 0.25 V [6] 50	0.83	2.44
PdCu	0.86 [6]	7.25×10^{-6} [6]	150 at 0.35 V [6] 187.5	0.90	0.89
Pd_5Cu_4Pt	0.95 [17]	6.80×10^{-4} [17]	325 at 0.45 V [17] 406.3	0.99	0.52

[a] Data extracted from MEAs in Refs. [6,17].

hydrated H^+ flowing through the Nafion and the resistance of the electron flowing through the electrode. The concentration losses come from a drop in the concentration of the reactants as they are consumed by the fuel cell [18]. The maximum power densities quoted in other polarization curves studies [6,17] (Table 2) differ from the data reported here; the main reason being a mass transfer effect. In the polarization experiments, the fuel cell electrodes were allowed to saturate with H_2 and O_2 for at least 10 min before each polarization scan. In the continuous 100 h testing, only the H_2 and O_2 molecules that actually reach the active sites can react. The values estimated for the resistances after the 100 h continuous fuel cell testing are collected in Table 1 (affected by the electrode geometrical area). These values are influenced by the three types of resistance losses mentioned above and are dominated by the mass transfer effect. Interestingly, the MEA2-BOL Pd cathode presents the highest resistance value, while the MEA6-BOL Pd_5Cu_4Pt presents the lowest value. For a quick overview of reference data, the ohmic resistances extracted from the reported plots of cell voltage versus current density by Martínez-Casillas et al. [17] are collected in Table 2. The ohmic resistances were estimated from the slope of the linear region of the plot cell voltage versus current density. These values were found to depend also upon cathode material; the calculated values point to a dual contribution of activation and ohmic losses. Interestingly, the Pd-cathode MEAs present the highest resistance values, while the Pd_5Cu_4Pt presents the lowest resistance, close to Pt/Pt MEA.

3.2. *Membrane electrode assembly SEM imaging*

Fig. 2 shows the SEM micrographs of the transversal section of MEAs. The as-prepared MEAs (Fig. 2(a)–(c)) present a compact, homogenous and thick layer of electrocatalysts. The electrocatalyst/membrane interface exhibits good contact. For the BOL-MEAs (Fig. 2(d)–(f)), the formation of cracks and random channels in the electrocatalyst layer becomes evident. These channels are necessary to improve the contact between the oxygen gas and the electrocatalyst nanoparticles, and also to remove the formed water. After 116 h of continuous operation, the electrocatalyst/membrane interface is separated in some areas (Fig. 2(d)). This can reduce the fuel cell performance at long term. The SEM pictures of new-MEAs and BOL-MEAs cathodes top view demonstrated that the spherical morphology and the aggregate size around 70 nm were independent of the electrocatalyst and both were maintained after continuous fuel cell testing (Supplementary file). The electrocatalyst particles + carbon vulcan + Nafion ionomer aggregate to from the electrode body. Carbon Vulcan is known to have a particle size about 40–60 nm, thus the aggregate size is dominated by this material.

3.3. *The central layer, SAXS of Nafion membrane*

Deviations from the optimum fuel cell operation conditions can lead to degradation of the MEA components. The Nafion membrane is well known to be stable but its stability might be compromised by the formation at cathode of HO• and HOO• radicals, or by cation contamination from the dissolution of electrocatalyst metals. The Nafion membrane is described as a tridimensional structure composed of ionic clusters ($-SO_3^-$ cavities) dispersed in a perfluorinated matrix ($-CF_2-CF_2-$ backbone) [3]. These structures are not accessible by SEM techniques, but well characterized by SAXS [3]. The SAXS features of Nafion membranes at low scattering vector (q) region have been interpreted as originating from a long chain polymer, i.e. a lamellar domain in the perfluorinated matrix ($-CF_2-CF_2-$ backbone). The feature at high-q region has been assigned to ionic cluster domains ($-SO_3^-$ cavities), i.e. the ionomer peak [3]. In the present work, the SAXS data were analyzed separately in the two q-regions; called hereafter the low-q and the high-q regions. Fig. 3 presents the experimental SAXS and the fitting of the dry Nafion membranes that are an integral part of the new and BOL-MEAs. Table 1 collects the size of both the lamellar and ionic cluster domains obtained from the model fitting.

3.3.1. *SAXS fitting at the low-q region (0.1–0.6 nm^{-1})*

The perfluorinated matrix was modeled as an ensemble of ellipsoid of revolution particles with uniform scattering length density [3,19]:

$$P(q,\alpha) = \frac{scale}{V} f^2(q) + bkg \quad (1)$$

$$f(q) = \frac{3(\Delta\rho)V(\sin(qR) - qR\cos(qR))}{(qR)^3} \quad (2)$$

$$R = R(R_a, R_b, \alpha) = \left(R_b^2 \sin^2\alpha + R_b^2 \cos^2\alpha\right)^{1/2} \quad (3)$$

where α is the angle between the axis of the ellipsoid and the scattering vector q, V is the volume of the ellipsoid, R_a and R_b are respectively the radius along and perpendicular to the rotation axis, $\Delta\rho$ is the scattering length density difference between the scatterer and the solvent (no solvent was involved here) and *scale* is a scaling factor [19,20]. Attempts to fit the data with others form factors did not succeed; the ellipsoid model is in agreement with the theoretical data reported by Schmidt-Rohr and Chen [21] and with the experimental data reported by Kim et al. [22], where elongated particles fit the Nafion backbone domains. However, the size of those domains is still under discussion, since the reported values range from 2–5 nm up to 50 nm, both theoretically and experimentally [21]. These values may dependent upon the polymer production process, supplier, activation and thermal history. A trend in reduction of the size for the lamellar domains upon fuel cell testing was confirmed by SAXS fitting (Table 1). No relationship between the cathode electrode material and the reduction of lamellar size was found. At the BOL, i.e. 116 h of fuel cell testing, the membrane was stable enough.

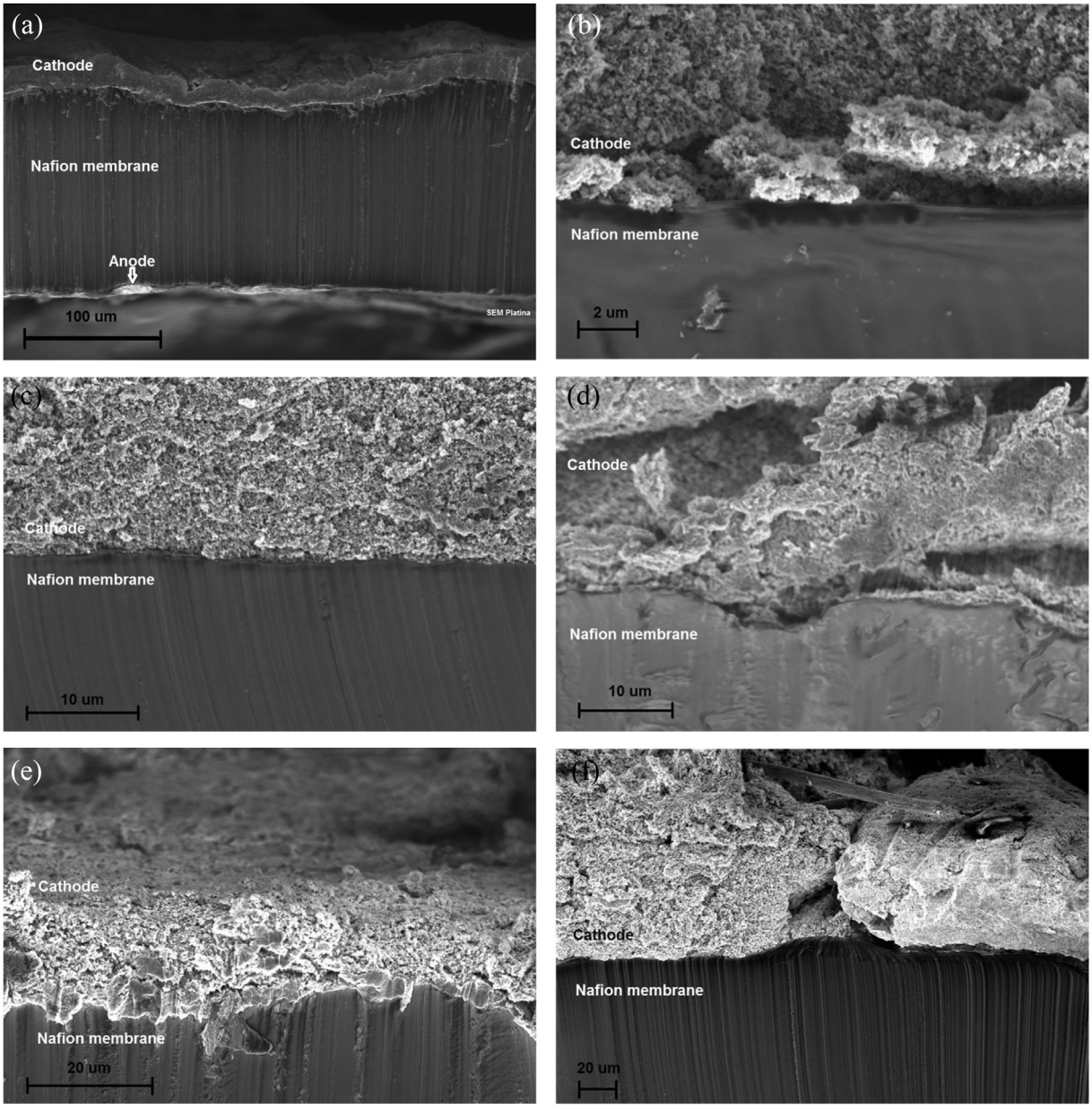

Fig. 2 – (a) SEM micrograph of the transversal section of MEA1-new; Pd cathode. (b) SEM micrograph of the transversal section of MEA3-new; PdCu cathode. (c) SEM micrograph of the transversal section of MEA5-new; Pd_5Cu_4Pt cathode. (d) SEM micrograph of the transversal section of MEA2-BOL; Pd cathode. (e) SEM micrograph of the transversal section of MEA4-BOL; PdCu cathode. (f) SEM micrograph of the transversal section of MEA6-BOL; Pd_5Cu_4Pt cathode.

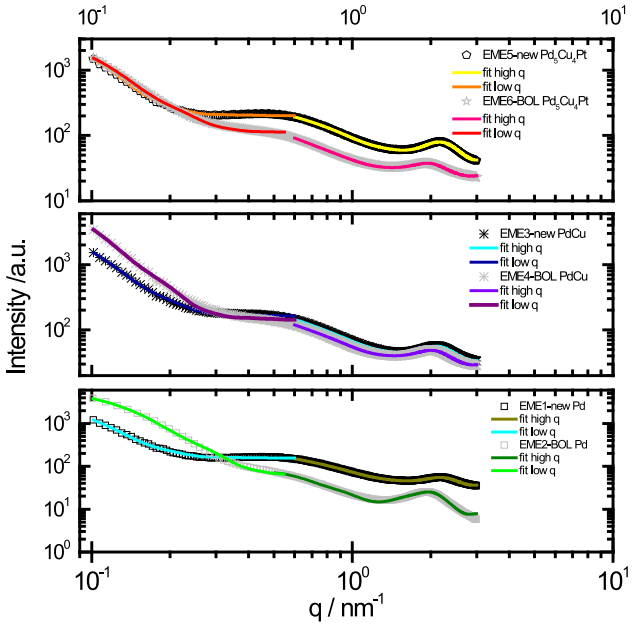

Fig. 3 – Small angle X-ray scattering of Nafion proton-conductive membrane.

But in the long term, a loss of the lamellar domains could lead to gas crossover and ultimately to fuel cell failure.

3.3.2. *SAXS fitting at the high-q region (0.6–2.99 nm^{-1})*

A spherical core–shell morphology has been frequently proposed as a model for the ionic cluster domains [3]. Here, the ionic cluster domain was best fitted as a cylinder core–-shell [3,20]:

$$f(q) = 2(\rho_c - \rho_s)V_c \frac{\sin\left(qL\cos\frac{\alpha}{2}\right)}{qL\cos\frac{\alpha}{2}} \frac{J_1(qr\sin\alpha)}{qr\sin\alpha} + 2(\rho_s - \rho_{solv})V_s \frac{\sin\left(q(L+t)\cos\frac{\alpha}{2}\right)}{q(L+t)\cos\frac{\alpha}{2}} \frac{J_1(q(r+t)\sin\alpha)}{q(r+t)\sin\alpha} \quad (4)$$

where α is the angle between the axis of the cylinder and the scattering vector q; V_c, L and r are respectively the volume, the length and the radius of the core; V_s and t are respectively the volume and the thickness of the shell; ρ_c and ρ_s are respectively the scattering length density of the core and the shell; ρ_{solv} is the scattering length density of the solvent however no solvent was involved here. J_1 is the first order Bessel function [3]. The core consists of cavities (full of water when hydrated) and the shell is related to the SO_3^- groups where the hydrated-proton conduction occurs. The position of the ionic cluster peak can vary around 1.5 nm^{-1} depending on the water content. It shifts to lower q with higher water content [3,23]. In the present materials, the ionic cluster peak is shifted up to 2.2 nm^{-1} in the as-prepared MEAs, in agreement with the severe dehydration of membrane that takes place during the hot-pressing step in the MEAs preparation. The ionic peak is shifted up to 1.9 nm^{-1} in the BOL-MEAs; following from the dry storage after fuel cell testing. The ionic cluster peak position in the BOL-MEAs indicates that some of the produced water is kept after fuel cell operation and dry storage. A quick correlation of the peak position with the water content [vol $\%_{water} = 46.49–67.44*\ln(q_{ionic\ peak})$] in the experimental data reported by Gierke et al. and re-printed by Schmidt-Rohr and Chen [21] leads to about 3%vol. water at the BOL-MEAs and lower values for new-MEAs. The size of the ionic cluster remains unchanged upon fuel cell continuous operation independently of the cathode-electrocatalyst material. Despite the dry condition of the membranes, the estimated size of the ionic cluster (diameter) remains adequate for water diffusion. The shape form and the estimated size are in agreement with the parallel water-channel model for Nafion proposed by Schmidt-Rohr and Chen [21]. In this model, the water diffuses through parallel channels of 2.4 nm of diameter in average (cylindrical inverted micelles of 1.8 nm–3.5 nm of diameter) stabilized in the outside by elongated backbone domains.

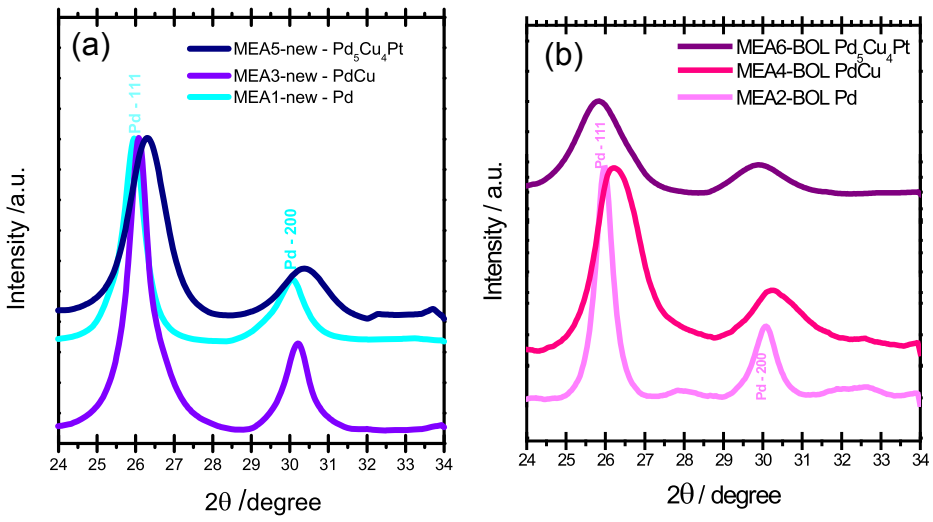

Fig. 4 – (a) Synchrotron radiation X-ray diffraction of "new MEAs" Pd, PdCu and Pd_5Cu_4Pt (λ = 1.008 A). (b) Synchrotron radiation X-ray diffraction of "BOLMEAs" Pd, PdCu and Pd_5Cu_4Pt (λ = 1.008 A).

3.4. *The cathode layer, electrocatalysts SR-XRD*

Fig. 4(a) and (b) presents the SR-XRD patterns of the cathode materials. Sample to detector distance set-up allowed detailed observation of XRD in a short diffraction angle range 2θ, i.e. where the (111) and (200) peaks of Pd are located. In such short 2θ range, the small shifts in the positions of the peaks and their broadening can be accurately quantified. The peaks (111) and (200) were used to calculate the nano-crystallite size [24], the crystal cell lattice size and bond distance [25] through refinement with the MAUD software. Structural data from SR-XRD is collected in Table 1.

3.4.1. *SR-XRD of cathode electrocatalysts at new MEAs*

In Fig. 4(a), the MEA1-new Pd pattern is characteristic of the cubic Pd structure, i.e. (111) and (200) peaks. The incorporation of Cu to Pd (MEA3-new PdCu) leads to a small shifting of peak positions towards higher 2θ values. This indicates a reduction in the size of the unit cell by Cu integration into the Pd matrix. Such a contraction was expected and already observed in Pd–Cu nanoparticles obtained by gas phase synthesis [26]. No indication of metallic Cu was found (the Cu (111) and (200) peaks were expected at 27.99° and 32.43° in 2θ respectively). Neither copper oxides nor Cu–Pd alloys were observed. The corresponding (111) and (200) peaks of MEA5-new Pd_5Cu_4Pt were observed at 26.29° and 30.35° respectively; they do not match with any of the reported Pt, Cu, PdCu, PtCu, PdPt or PdCuPt alloys. The X-ray diffraction pattern of MEA5-new Pd_5Cu_4Pt is consistent with a contraction in crystal cell lattice. The lattice contraction is not an expected effect of the incorporation of a "bulky" atom such as Pt. Instead it is explained as an effect of nanoparticle formation, as an effort to decrease the nanoparticle surface energy [27]. Martínez-Casillas et al. already described the as-prepared Pd_5Cu_4Pt nanoparticles as a non-equilibrium alloy of cubic symmetry with uniform distribution of Pd, Cu and Pt, with diameters between 2 and 3 nm [17]; the Pd_5Cu_4Pt diameter being slightly smaller than the one of Pd or PdCu [6,7]. The same trend in nano-crystallite size Pd > PdCu > Pd_5Cu_4Pt at new-MEAs was found in the present work, see Table 1. Then, it can be concluded that the unexpected lattice contraction (and thus bond distance) is a result of the formation of particles in the nanometer range.

3.4.2. *SR-XRD of cathode electrocatalysts at BOL-MEAs*

Fig. 4(b) presents the X-ray diffraction pattern of the BOL-MEAs cathode materials. The MEA2-BOL Pd pattern agrees with the characteristic cubic Pd structure. MEA4-BOL PdCu shows the same shift as in the MEA3-new PdCu, in agreement with the incorporation of Cu into Pd matrix. The corresponding (111) and (200) peaks of MEA6-BOL Pd_5Cu_4Pt are located at 25.84° and 29.88° in 2θ respectively, indicating the increase of Pd–Pd bond distance and crystal lattice induced by fuel cell testing. Segregation of materials and formation of noble metal rich skin are expected under the temperature, gas pressure and overpotential within the operating fuel cell. Pt-skinned materials are well known to have high activity towards the ORR. On the other hand, Krüger et al. [27] identify the surface oxidation of Pd nanoclusters as a way to reduce the surface energy. As a result, an increase of Pd–Pd bond distance is expected. The ORR is a surface reaction that involves the adsorption of oxygen and the formation of oxygenated intermediaries (–OH and –OOH), as a result the increase in crystal cell lattice was observed. Relaxing the Pd_5Cu_4Pt lattice provides the right geometric environment for efficient ORR. This process is known as the electrochemical activation of electrocatalyst and took place in the fuel cell during the heating-up and gas pressure setting by application of pulse or step potentials. Both effects, i.e. the re-ordering of Pd_5Cu_4Pt and surface oxides formation, can play an important role in the activity towards the ORR. Finally, a marked reduction of nanocrystal domains size of Pd nanoparticles from about 4 nm to 2 nm was observed as an effect of fuel cell testing. A similar effect but less pronounced was found for

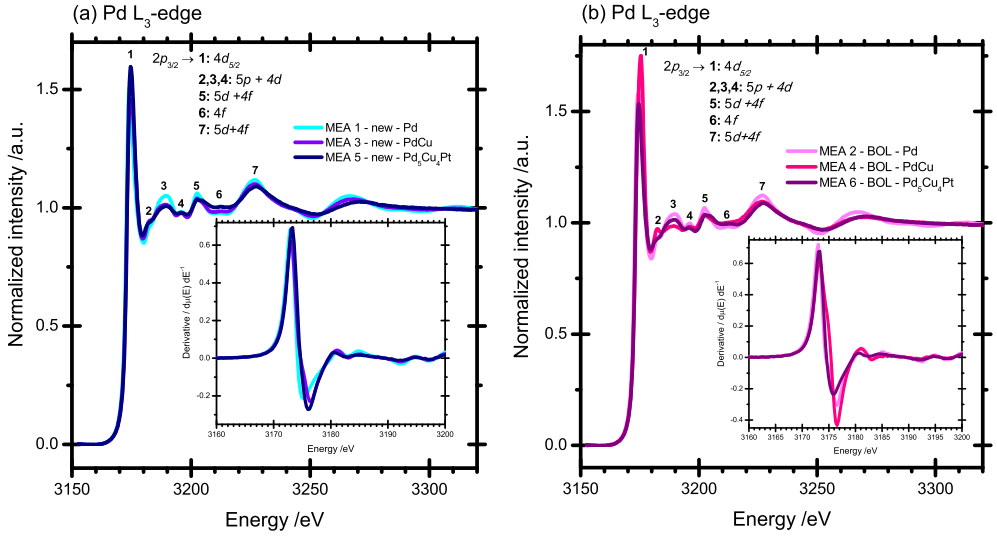

Fig. 5 – (a) Pd L_3-edge X-ray absorption spectra of Pd, PdCu and Pd_5Cu_4Pt "new MEAs". Inset: the derivative of the fluorescence signal. (b) Pd L_3-edge X-ray absorption spectra of Pd, PdCu and Pd_5Cu_4Pt beginning of life "BOLMEAs". Inset: the derivative of the fluorescence signal.

PdCu nanoparticles, while the Pd_5Cu_4Pt size remained practically constant (Table 1).

3.5. *The cathode layer, electrocatalysts XAS*

3.5.1. *Pd L_3-XAS at new and BOL MEAs*

Despite the importance of Pd as electrocatalyst, no comprehensive literature on Pd L_3-edge is yet available. Sham [28] has established the basis for the interpretation of the metallic Pd L_3-edge. The oscillatory features above the edge have been assigned as: peak 1 (white line) $2p_{3/2} \rightarrow 4d_{5/2}$ transition. The peaks 2, 3 and 4 are transitions to hybrid states with 5*p* and 4*d* character (*pd*), the peak 3 being the primary 5*p* state. The peaks 5, 6 and 7 are the result of the strong interaction between the 4*f* and 5*d* bands [28].

Fig. 5(a) presents the Pd L_3-edge XAS of the new MEAs. The spectra were normalized to the edge jump. An edge shift of +0.3 eV relative to E_0 of Pd was found for PdCu and Pd_5Cu_4Pt. Upon alloying, a reduction of $2p \rightarrow 5p$ transition was observed. Small changes of peaks 2, 3 and 4 became more noticeable in the inset plots that show the derivative of the fluorescence signal, where the strongest changes are for peak 3 ($2p \rightarrow 5p$ transition). Alloying of Pd with Cu and Pt introduces changes to the electronic and geometric structure that alter both the Pd *d*-band width and the Pd *d*-band center [29]. The increase in the intensity, width, and area of the white-line or even more its relationship with L_2-edge peak-area have been associated to the decrease in the occupancy of *d*-band in alloys of Pt (mainly) and some (scarce) examples of Au, Ni and Pd [28,30–34]. Considering the similarities in the nanoparticle synthesis, MEA production, fuel cell operation and XAS data collection and treatment, the trend in the integrated white peak area (−10 eV to +13 eV relative to E_0 [33,35]) was significant, and found to be: Pd ≈ PdCu < Pd_5Cu_4Pt for the as-prepared MEAs. This indicates a reduction of the occupancy of *d*-band of Pd upon alloying.

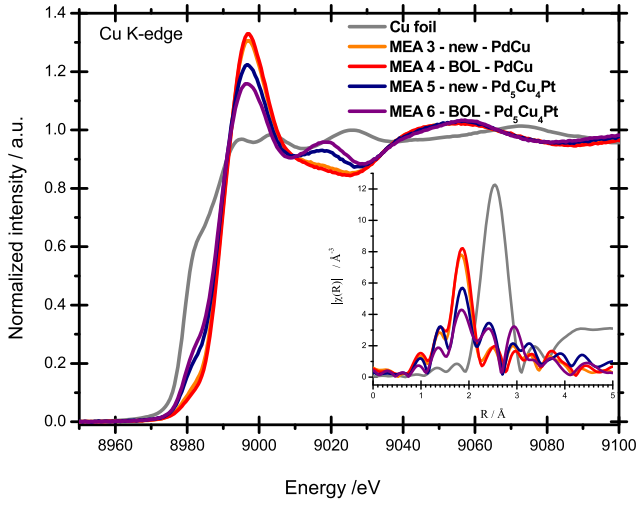

Fig. 6 – Cu K-edge X-ray absorption spectra of PdCu and Pd_5Cu_4Pt "new" and beginning of life "BOLMEAs". Inset: Fourier transformed EXAFS modulation with phase correction in the k-range of 2.0–11.5 $Å^{-1}$, k^2-weighted.

Fig. 5(b) presents the Pd L_3-edge XAS of the BOL MEAs. The edge shift of +0.3 eV relative to E_0 of Pd was conserved for PdCu and Pd_5Cu_4Pt after fuel cell performance testing. The trend in the integrated white peak area (or the vacancy) was Pd_5Cu_4Pt < Pd ≈ PdCu for the BOL-MEAs. The ORR towards water production involves the transfer of $4e^-$ per molecule of oxygen; from the cathode electrocatalyst to the oxygen and oxygenated intermediaries. The electrochemically activated Pd_5Cu_4Pt at MEA6-BOL can act as electron reservoir for the ORR, providing the appropriate electronic environment. The changes in the white line and oscillatory features (peaks 2, 3 and 4) also indicate a re-ordering in the Pd_5Cu_4Pt to some degree, in agreement with the findings of SR-XRD; but the limited k-range in the Pd L_3-edge is not sufficient to quantify structural changes. The distribution of the metals within the nanoparticles may be a key factor in the catalytic behavior according to the specific role of each component [36]. Because of that fact, XAS data collection at the Cu–K edge and Pt L_3-edge were performed.

3.5.2. *Cu K-XAS at new and BOL MEAs*

Fig. 6 presents the Cu K-edge spectra of PdCu and Pd_5Cu_4Pt new and BOL MEAs. The Cu K-edge features of new vs. BOL MEAs are essentially invariant with the fuel cell operation. As a reference, the Cu K-edge spectrum of a Cu-foil was included. The inset shows the Fourier transformed EXAFS modulation with phase correction in the k-range of 2.0–11.5 $Å^{-1}$ (k^2-weighted).

The $1s \rightarrow 4p$ transition was assigned to the first inflection point in the Cu-foil spectrum [37–40], i.e. the rise of the shoulder at 8980 eV. The $1s \rightarrow 4p$ transition intensity is Cu > Pd_5Cu_4Pt > PdCu in both new and BOL MEAs. The comparison of PdCu and Pd_5Cu_4Pt BOL MEAs at the Pd L_3-edge indicates an increase of the occupancy of *d*-band of Pd in Pd_5Cu_4Pt upon re-ordering. This means that a charge transfer towards Pd occurs. The comparison of PdCu and Pd_5Cu_4Pt BOL MEAs at the 1*s* to 4*p* transition at Cu K spectra indicates a reduction of the occupancy of *p* orbitals of the metallic Cu in Pd_5Cu_4Pt, i.e. a charge transfer from metallic Cu.

The magnitude and shape of pre-edge (if any) [37,40] and the region above the edge (5–25 eV) [33] have been related to the oxidation state of Cu and the Cu band vacancies. The shift of the Cu K-edge, the white-line between 8984 and 9007 eV and the peak between 9010 and 9028 eV are all features characteristic of Cu(II) compounds [41]. The white-line intensities of PdCu and Pd_5Cu_4Pt indicate that different proportions of Cu(II) compounds are formed, affected by the Pt neighboring.

Fourier transformed EXAFS inset shows peaks at: 1) 1.8 Å that can be related to Cu–O bond [42]; 2) 2.5 Å that is the Cu–Cu bond in Cu foil and 3) peaks at 2.4 and 2.9 Å that can be associated respectively to the Cu–Cu bond distortion by nanoparticle formation and to alloy formation, i.e. the interaction Cu–Pt [36] or Cu–Pd. The Cu in the electrocatalysts is described as a nano-mixture of amorphous CuO, metallic Cu and Cu–Pd/Cu–Pd–Pt alloy. The present and reported [6,7] XRD did not show formation of crystalline CuO; however Cu K-edge XANES and Fourier transformed EXAFS are consistent with partial formation of CuO. Interestingly, CuO is reported as a catalyst or catalyst precursor in many chemical reactions

that involve hydrogen as a reactant or a product, for example: $CO + 2H_2 \rightarrow CH_3OH$, $CO_2 + 3H_2 \rightarrow CH_3OH + H_2O$ or $NO + H_2 \rightarrow 1/2N_2 + H_2O$ [43]. Moriya et al. [44] identified the increase of CuO content with the increase of catalytic activity of Cu–Pt nanoparticles for the oxidation of CO to CO_2; where the adsorbed CO at Pt–Cu reacts with the active oxygen provided by the neighboring CuO. For the ORR the Pt or Pd active metal centers could interact with the O of CuO and the H^+ coming from the anode. The bond energy of Cu–O is almost the half of O=O (269 kJ mol^{-1} vs. 494 kJ mol^{-1} respectively) [45]. Thermodynamically, breaking the Cu–O bond must be favored over breaking the O=O. Thus CuO can be a promoter of the ORR, bringing its O to the Pt or Pd active metal and then re-adsorbing more O.

3.5.3. *Pt L_3-XAS at new and BOL MEAs*

Fig. 7 presents the Pt L_3-edge spectra of Pd_5Cu_4Pt MEAs. In absence of Pt-foil, the spectrum of the anode of MEA1-new, commercial nanoparticles of Pt (ETEK), was taken as reference for alloy formation. The new and BOL Pd_5Cu_4Pt MEAs display the same profile as Pt commercial nanoparticles. As stated above, the XAS was performed in the cathode side in fluorescence mode; however these spectra are the result of the additive responses of the Pd_5Cu_4Pt at the cathode and the Pt at the anode, the latter giving the primary contribution to the signal. In this way, data collection without MEA disassembling was not possible.

As an alternative, Pt L_3-edge spectra of the as-synthesized Pd_5Cu_4Pt powder were collected and averaged (green line of Fig. 7). This spectrum is equivalent to the cathode signal of MEA5-new Pd_5Cu_4Pt. The Pt-L_3 XAS oscillations are more clearly visible in the large inset of Fig. 7. The white-line is due to $2p_{2/3}$ to 5*d* transitions and its intensity is related to the Pt 5*d* vacancies [33,46]. Alterations in the Pt white-line have been attributed to two effects: 1) decrease of particles size and 2) alloying with a transition metal [33,47]. Both effects are observed in the Pd_5Cu_4Pt: 1) Martínez-Casillas et al. [17] already demonstrated that the as-synthesized Pd_5Cu_4Pt particles have a size between 2 and 3 nm, comparable to the particle size of commercial Pt black [48]. Additionally, the Pt in the Pd_5Cu_4Pt nanoparticles constitutes only a small fraction, leading to very small Pt domains. 2) Alloying must promote a charge transfer from metallic Cu to Pt that results in the reduction of Pt 5*d* vacancies. The small inset in Fig. 7 presents the Fourier transformed EXAFS modulation with phase correction in the k-range of 2.0–14 $Å^{-1}$ (k^3-weighted). The peak at 2.8 Å agrees well with the Pt–Pt bond distance, however the 2.5 Å peak is at a shorter distance than the expected 2.6 Å for the usual Pt–Cu [33]. The Pt L_3-edge XAS of as-synthesized Pd_5Cu_4Pt is in agreement with the contracted cell lattice observed by SR-XRD in MEA5-new. Bond length contraction is well documented for Pt and Au particles as a result of nano-size domain formation (1–10 nm) [47,49]. This phenomenon is particularly important for sizes below 3 nm [47].

Linear combination fitting of the MEA5-new gives a relation: μ(MEA5) = 0.989*μ(anode-MEA1-new) + 0.011*μ(Pd_5Cu_4Pt-powder); between −20 and 100 eV vs E_0, *R*-factor = 0.000039 (Athena software). The difference in the normalized $\mu(E)$ were extracted and the contribution of Pd_5Cu_4Pt was isolated (Fig. 8). The ΔXANES have been successfully used to obtain information of absorbed species over electrocatalysts surfaces [50]. Pd and Cu are species that modify the Pt surroundings and the catalyst surface, as the absorbed species also do. The mathematical description of the observed ΔXANES (and its components) in this ternary electrocatalyst requires a dedicated study; our aim here is just to describe the changes of Pd_5Cu_4Pt electrocatalyst before and after fuel cell testing. The profile of Pd_5Cu_4Pt at MEA5-new below 11,570 eV reflects a

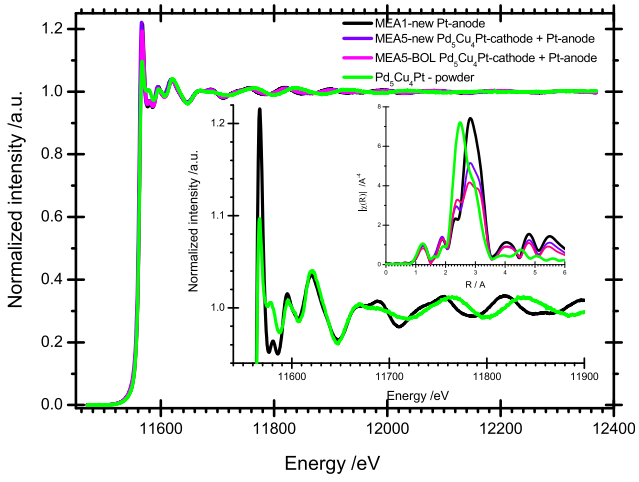

Fig. 7 – Pt L_3-edge X-ray absorption spectra of Pd_5Cu_4Pt "new" and beginning of life "BOLMEAs", Pt anode (MEA-1) and Pd_5Cu_4Pt powder. Inset 1: Detail of the Pt L_3-edge. Inset 2: Fourier transformed EXAFS modulation with phase correction in the k-range of 2.0–14 $Å^{-1}$, k^3-weighted. (For interpretation of the references to color in this figure legend, the reader is referred to the web version of this article.)

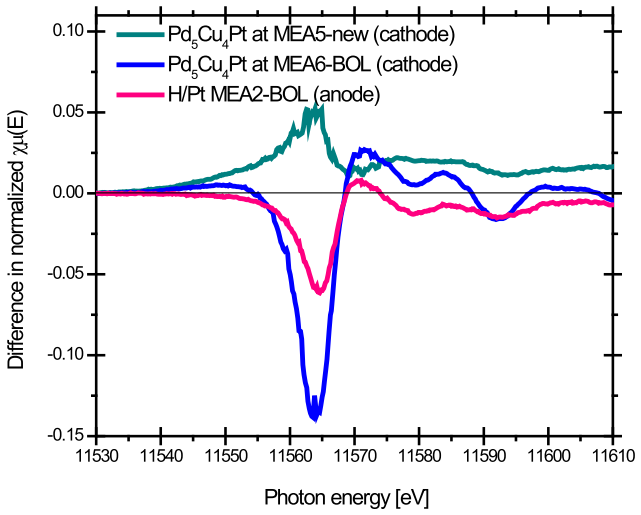

Fig. 8 – ΔXANES of Pd_5Cu_4Pt at MEA5-new – Pt at MEA1-new (light blue); Pd_5Cu_4Pt at MEA6-BOL – Pt at MEA2-BOL (blue) and Pt at MEA2-BOL – Pt at MEA1-new. (For interpretation of the references to color in this figure legend, the reader is referred to the web version of this article.)

shift in the edge position towards low energy; whereas the profile of Pd_5Cu_4Pt at MEA5-BOL returns to high energy, closer to the Pt nanoparticles. The increase of intensity in the negative part below 11,570 eV of Pd_5Cu_4Pt at MEA5-BOL indicates a reduction of the Pt 5*d* band vacancy vs Pt nanoparticles. The Pt can serve as electron reservoir during the ORR. The oscillations after 11,570 correlate with the changes induced by Pd and Cu neighboring, consistent with the SR-XRD and Pd L_3 XAS findings.

3.6. *The anode layer, electrocatalysts Pt L_3-XAS*

Fig. 8 includes the ΔXANES of the Pt nanoparticles at the anode side. The normalized $\mu(E)$ signal of the Pt nanoparticles from the anode of MEA1-new was removed from the normalized $\mu(E)$ signal of the anode of MEA2-BOL. This ΔXANES is consistent with atomic hydrogen absorbed at the Pt nanoparticle surface [50], according to the hydrogen oxidation reaction that takes place at the anode. No further changes were observed in the anode after fuel cell testing.

4. Conclusions

Novel Pd, PdCu and Pd_5Cu_4Pt electrocatalysts were synthesized and PEM fuel cell based on these materials were tested. The incorporation of Cu to Pd reduces the load of the noble metal and improves the fuel cell performance. Incorporation of Pt even in small quantities increases the fuel cell performance. SEM micrographs of the transversal section of BOL-MEAs indicated the formation of cracks and random channels in the cathode electrocatalyst layer, necessary for an adequate gas-in and water-out flow. A separation of electrocatalyst/membrane interface was found in some places after fuel cell continuous testing.

The effects of fuel cell operating conditions on the proton exchange membrane Nafion was tested by means of small angle X-ray scattering. The SAXS profiles were divided in two regions for analysis. The fitting of the low *q*-region indicates a decrease of lamellar size by fuel cell continuous operation. The fitting of the high *q*-region indicates that the size of the ionic cluster does not change with fuel cell continuous operation.

Synchrotron radiation X-ray diffraction experiments confirmed the introduction of Cu into Pd lattice in the PdCu electrocatalyst. In the Pd_5Cu_4Pt electrocatalyst of as-prepared MEA an unexpected decrease in crystal lattice was found. Relaxation of the crystal lattice of Pd_5Cu_4Pt was found after electrochemical activation and fuel cell testing; giving an adequate geometry for ORR as indicated by fuel cell performance.

The outlined X-ray absorption spectroscopy studies at the cathode sides reflect the changes in the electronic and local geometric environments of Pd, PdCu and Pd_5Cu_4Pt electrocatalysts. The most interesting metal–metal interactions at the electrocatalyst were found after electrochemical activation and fuel cell testing, i.e. the BOL MEAs. The X-ray absorption spectroscopy experiments at the Pd L_3, Cu K and Pt L_3-edge lead to conclude that: 1) there is a change in electronic environment due to charge transfer Cu to Pd/Pt. In turn, the noble metals Pd and Pt act as an electron reservoir for the ORR. 2) The Cu in the electrocatalyst can be described as a nano-mixture of metallic Cu, alloyed Cu and CuO. The CuO acts as a promoter of the ORR. 3) Re-organization or relaxing of crystal cell lattice of Pd_5Cu_4Pt electrocatalyst occurs. All these combined effects are favorable for the ORR.

Acknowledgments

The authors are grateful to CINVESTAV and MAX-Lab. The Authors acknowledge the advice of Dr. Stefan Carlson and Dr. Katarina Norén during XAS data collection and of Dr. Tomás Plivelic and Dr. Ana Labrador during SAXS data collection. KSA and SEC were supported by the Swedish Research Council and the Crafoord Foundation. DCMC thanks Mexico's National Council of Science and Technology, CONACYT, for the doctoral fellowship. TP and KBZ are grateful for financial support of the Knut and Alice Wallenberg Foundation and Swedish Energy Agency. Collaboration within nmC@LU is acknowledged.

Appendix A. Supplementary data

Supplementary data related to this article can be found at http://dx.doi.org/10.1016/j.ijhydene.2014.01.056.

REFERENCES

[1] Shen PK. PEM fuel cell catalyst layers and MEAs. In: Zhang J, editor. PEM fuel cell electrocatalysts and catalyst layers fundamentals and applications. London: Springer-Verlag; 2008. pp. 355–68.
[2] Danilczuk M, Coms FD, Schlick S. Visualizing chemical reactions and crossover processes in a fuel cell inserted in the ESR resonator: detection by spin trapping of oxygen radicals, Nafion-derived fragments, and hydrogen and deuterium atoms. J Phys Chem B 2009;113:8031–42.
[3] Tsao CS, Chang HL, Jeng US, Lin JM, Lin TL. SAXS characterization of the Nafion membrane nanostructure modified by radiation cross-linkage. Polymer 2005;46:8430–7.
[4] Shao M, Liu P, Zhang J, Adzic R. Origin of enhanced activity in palladium alloy electrocatalysts for oxygen reduction reaction. J Phys Chem B 2007;111:6772–5.
[5] Salvador-Pascual JJ, Citalan-Cigarroa S, Solorza-Feria O. Kinetics of oxygen reduction reaction on nanosized Pd electrocatalyst in acid media. J Power Sources 2007;172:229–34.
[6] Martínez-Casillas DC, Vázquez-Huerta G, Pérez-Robles JF, Solorza-Feria O. Electrocatalytic reduction of dioxygen on PdCu for polymer electrolyte membrane fuel cells. J Power Sources 2011;196:4468–74.
[7] Martínez-Casillas DC, Gil-Esquivel OA, Solorza-Feria O. Thermal treatment effects on Pd_5Cu_4Pt electrocatalyst for the oxygen reduction reaction in a PEM fuel cell. J New Mater Electrochem Syst 2012;15(3):145–9.
[8] Prabhuram J, Zhao TS, Liang ZX, Yang H, Wong CW. Pd and Pd–Cu alloy deposited Nafion membranes for reduction of methanol crossover in direct methanol fuel cells. J Electrochem Soc 2005;52(7):A1390–7.

[9] González-Huerta RG, Guzman-Guzman A, Solorza-Feria O. Optimization of Ru_xSe_y electrocatalyst loading for oxygen reduction in a PEMFC. Int J Hydrogen Energy 2010;35(21):12115–9.

[10] Mammen CB, Ursby T, Thunnissen M, Als-Nielsen J. Bent diamond crystals and multilayer based optics at the new 5-station protein crystallography beamline 'Cassiopeia' at MAX-lab. AIP Conf Proc 2004;705:808–11.

[11] Mammen CB, Ursby T, Cerenius Y, Thunnissen M, Als-Nielsen J, Larsen S, et al. Design of a 5-station macromolecular crystallography beam line at MAX-Lab. Acta Phys Pol A 2002;101:595–602.

[12] Cerenius Y, Ståhl K, Svensson LA, Ursby T, Oskarsson Å, Albertsson J, et al. The crystallography beamline I711 at MAX II. J Synchrotron Rad 2000;7:203–8.

[13] Hammersley AP, Svensson SO, Hanfland M, Fitch AN, Häusermann D. Two-dimensional detector software: from real detector to idealized image or two-theta scan. High Press Res 1996;14:235–48.

[14] Grehk TM, Nilsson PO. The design of the material science beamline, I811, at MAX-II. Nucl Instr Meth Phys Res 2001;467–468:635–8.

[15] Carlson S, Clausen M, Gridneva L, Sommarin B, Svensson C. XAFS experiments at beamline I811, MAX-lab synchrotron source, Sweden. J Synchrotron Rad 2006;13:359–69.

[16] Ravel B, Newville M. ATHENA, ARTEMIS, HEPHAESTUS: data analysis for X-ray absorption spectroscopy using IFEFFIT. J Synchrotron Radiat 2005;12:537–41.

[17] Martínez-Casillas DC, Calderon H, Collins-Martínez V, Solorza-Feria O. Pd_5Cu_4Pt oxygen reduction nanocatalyst for PEM fuel cells. Int J Hydrogen Energy 2013;38:12674–80.

[18] Yuan XZ, Wang H. PEM fuel cell fundamentals. In: Zhang J, editor. PEM fuel cell electrocatalysts and catalyst layers fundamentals and applications. London: Springer-Verlag; 2008. pp. 67–70.

[19] Feigin LA, Svergun DI. Structure analysis by small-angle X-ray and neutron scattering. New York: Plenum Press; 1987.

[20] Glatter O. Interpretation. In: Glatter O, Kratky O, editors. Small angle X-ray scattering. London: Academic Press; 1982. pp. 167–96.

[21] Schmidt-Rohr K, Chen Q. Parallel cylindrical water nanochannels in Nafion fuel-cell membranes. Nat Mater 2008;7:75–83.

[22] Kim MH, Glinka CJ, Grot SA, Grot WG. SANS study of the effects of water vapor sorption on the nanoscale structure of perfluorinated sulfonic acid (NAFION) membranes. Macromolecules 2006;39:4775–87.

[23] Haubold HG, Vad T, Jungbluth H, Hiller P. Nano structure of Nafion: a SAXS study. Electrochim Acta 2001;46:1559–63.

[24] Cullity BD, Stock SR. Elements of X-ray diffraction. 3rd ed. London: Prentice-Hall; 2001.

[25] Massa W. Crystal structure determination. Berlin: Springer; 2000.

[26] Sengar SK, Mehta BR, Gupta G. Charge transfer, lattice distortion, and quantum confinement effects in Pd, Cu, and Pd–Cu nanoparticles; size and alloying induced modifications in binding energy. Appl Phys Lett 2011;98:193115–23.

[27] Krüger S, Vent S, Nörtemann F, Staufer M, Rösch N. The average bond length in Pd clusters Pd_n, $n = 4–309$: a density-functional case study on the scaling of cluster properties. J Chem Phys 2001;115:2082–7.

[28] Sham TK. L-edge X-ray-absorption systematics of the noble metals Rh, Pd, and Ag and the main-group metals in and Sn: a study of the unoccupied density of states in 4d elements. Phys Rev B 1985;31:1888–902.

[29] Hammer B. Special sites at noble and late transition metal catalysts. Top Catal 2006;37:3–16.

[30] Jeon J, Chen J, Croft M. X-ray-absorption studies of the d-orbital occupancies of selected 4d/5d transition metals compounded with group-III/IV ligands. Phys Rev B 1994;50:6555–63.

[31] Sham TK. L-edge X-ray-absorption spectra of $PdA1_3$ and $PdCl_2$. A study of charge redistribution in compounds of an element with a nearly full 4d shell. Phys Rev B 1985;31:1903–8.

[32] Sham TK. X-ray absorption studies of unoccupied d-band states in gold and nickel metallic compounds. Solid State Commun 1987;64:1103–6.

[33] Dutta I, Carpenter MK, Balogh MP, Ziegelbauer JM, Moylan TE, Atwan MH, et al. Electrochemical and structural study of a chemically dealloyed PtCu oxygen reduction catalyst. J Phys Chem C 2010;114:16309–20.

[34] Mansour AN, Cook Jr JW, Sayers DE. Quantitative technique for the determination of the number of unoccupied d-electron states in a platinum catalyst using the $L_{2,3}$ X-ray absorption edge spectra. J Phys Chem 1984;88:2330–4.

[35] Mukerjee S, Srinivasan S, Soriaga MP, McBreen J. Effect of preparation conditions of Pt alloys on their electronic, structural, and electrocatalytic activities for oxygen reduction-XRD, XAS, and electrochemical studies. J Phys Chem 1995;99:4577–89.

[36] Fernandez-Garcıa M, Conesa JC, Clotet A, Ricart JM, Lopez N, Illas F. Study of the heterometallic bond nature in PdCu(111) surfaces. J Phys Chem B 1998;102:141–7.

[37] Behrens P. X-ray absorption spectroscopy in chemistry II. X-ray absorption near edge structure. Trends Anal Chem 1992;11(7):237–44.

[38] Smith TA, Penner-Hahn JE, Berding MA, Doniach S, Hodgson KO. Polarized X-ray absorption edge spectroscopy of single-crystal copper (II) complexes. J Am Chem Soc 1985;107:5945–55.

[39] Kau LS, Spira-Solomon DJ, Penner-Hahn JE, Hodgson KO, Solomon EI. X-ray absorption edge determination of the oxidation state and coordination number of copper: application to the type 3 site in *Rhus vernicifera* laccase and its reaction with oxygen. J Am Chem Soc 1987;109:6433–42.

[40] Grunes LA. Study of the K edges of 3d transition metals in pure and oxide form by X-ray-absorption spectroscopy. Phys Rev B 1983;27:2111–31.

[41] Gomes WCM, Wanderley-Neto AC, Mendonca-Pimentel P, Araújo-Melo DM, Goncalves-e-Silva FR. An in situ X-ray absorption spectroscopy study of copper nanoparticles in microemulsion. Colloids Surf Physicochem Eng Asp 2013;426:18–25.

[42] Molenbroek AM, Haukka S, Clausen BS. Alloying in Cu/Pd nanoparticle catalysts. J Phys Chem B 1998;102:10680–9.

[43] Kim JY, Rodriguez JA, Hanson JC, Frenkel AI, Lee PL. Reduction of CuO and Cu_2O with H_2: H embedding and kinetic effects in the formation of suboxides. J Am Chem Soc 2003;125:10684–92.

[44] Moriya T, Kugai J, Seino S, Ohkubo Y, Nakaga-Nakagawa T, Nitani H, et al. CuO role in c-Fe_2O_3-supported Pt–Cu bimetallic nanoparticles synthesized by radiation-induced reduction as catalysts for preferential CO oxidation. J Nanopart Res 2013;15:1451–6.

[45] Huheey JE, Keiter EA, Keiter RL. Inorganic chemistry: principles of structure and reactivity. 4th ed. USA: HarperCollins College Publishers; 1993.

[46] Merte LR, Behafarid F, Miller DJ, Friebel D, Cho S, Mbuga F, et al. Electrochemical oxidation of size-selected Pt nanoparticles studied using in situ high-energy-resolution X-ray absorption spectroscopy. ACS Catal 2012;2:2371–6.

[47] Lei Y, Jelic J, Nitsche LC, Randall M, Miller J. Effect of particle size and adsorbates on the L_3, L_2 and L_1 X-ray absorption near edge structure of supported Pt nanoparticles. Top Catal 2011;54:334–48.

[48] Mukerjee S. McBreen effect of particle size on the electrocatalyst by carbon-supported Pt electrocatalysts: an in situ XAS investigation. J Electroanal Chem 1998;448:163–71.
[49] Szczerba W, Riesemeier H, Thünemann AF. Bond length contraction in gold nanoparticles. Anal Bioanal Chem 2010;398:1967–72.
[50] Ramaker DE, Koningsberger DC. The atomic AXAFS and ΔμXANES techniques as applied to heterogeneous catalysis and electrocatalysis. Phys Chem Chem Phys 2010;12:5514–34.